remote sensing

MDPI

Article

Analysis of the Anomalous Environmental Response to the 2022 Tonga Volcanic Eruption Based on GNSS

Maosheng Zhou [1], Hao Gao [1,2], Dingfeng Yu [1,*], Jinyun Guo [2], Lin Zhu [1], Lei Yang [1] and Shunqi Pan [3]

[1] Institute of Oceanographic Instrumentation, Qilu University of Technology (Shandong Academy of Sciences), Qingdao 266101, China
[2] College of Geodesy and Geomatics, Shandong University of Science and Technology, Qingdao 266590, China
[3] Hydro-Environmental Research Centre, School of Engineering, Cardiff University, Cardiff CF24 3AA, UK
* Correspondence: dfyu@qlu.edu.cn

Abstract: On 15 January 2022, a violent eruption and tsunami of the Hunga Tonga-Hunga Ha'apai (HTHH) volcano in Tonga, South Pacific, caused widespread international concern. In order to detect the anomalous environmental response caused by the HTHH volcanic eruption based on GNSS ionospheric data, GNSS tropospheric data and GNSS coordinate time series, a new method combining the zenith non-hydrostatic delay difference method and the extreme-point symmetric mode decomposition (ESMD) method, was proposed to detect tropospheric anomalies. The moving interquartile range method and the ESMD method were introduced to detect ionospheric anomalous and coordinate time series anomalies, respectively. The results showed that 9–10 h before the eruption of the Tonga volcano and 11–12 h after the eruption of the Tonga volcano, obvious total electron content (TEC) anomalies occurred in the volcanic eruption center and its northeast and southeast, with the maximum abnormal value of 15 TECU. Significant tropospheric anomalies were observed on the day of the HTHH volcano eruption as well as 1–3 days and 16–17 days after the eruption, and the abnormal intensity was more than 10 times that of normal. The coordinate time series in direction E showed very significant anomalies at approximately 2:45 p.m. on 14 January, at approximately 4:30 a.m.–5:40 a.m. on 15 January, and at approximately 3:45 a.m. on 16 January, with anomalies reaching a maximum of 7–8 times daily. The abnormality in the direction north (N) is not obvious. Very prominent anomalies can be observed in the direction up (U) at approximately 4:30 a.m.–5:40 a.m., with the intensity of the anomalies exceeding the normal by more than 10 times. In this study, GNSS was successfully used to detect the anomalous environmental response during this HTHH volcano eruption.

Keywords: Tonga submarine volcano eruption; global navigation satellite system; ionospheric anomalies; tropospheric anomalies; ground position anomalies

Citation: Zhou, M.; Gao, H.; Yu, D.; Guo, J.; Zhu, L.; Yang, L.; Pan, S. Analysis of the Anomalous Environmental Response to the 2022 Tonga Volcanic Eruption Based on GNSS. *Remote Sens.* **2022**, *14*, 4847. https://doi.org/10.3390/rs14194847

Academic Editor: Jonathan Procter

Received: 23 July 2022
Accepted: 24 September 2022
Published: 28 September 2022

1. Introduction

On 15 January 2022, a violent volcanic eruption and tsunami occurred at the Hunga Tonga—Hunga Ha'apai (HTHH) submarine volcano (175°23′58.54″W, 20°30′57.78″S), approximately 65 km north of Nuku'alofa, the capital of the South Pacific island nation of Tonga. Tsunami warnings were issued in Australia, Japan, the USA, and Chile on the Pacific coast. The volcanic eruption produced large quantities of ash, gas, and water vapour [1,2]. This was the most violent eruption of the HTHH underwater volcano since 1100 AD [3], attracting widespread attention worldwide. Volcanic eruptions are a manifestation of the movement of the earth's crust and the release of energy from the earth's interior at the surface, while more than 70% of all volcanic activity on earth occurs on the submarine [4]. The monitoring of submarine volcanic activity and the study of environmental responses during volcanic eruptions not only are beneficial to the understanding of crustal movements and the mechanism of interaction between circles but also have great significance for the prevention and control of volcanic hazard risks.

Volcanic eruptions are often accompanied by strong seismic activity, which not only causes displacement of the crust but also affects the ionosphere and upper atmosphere. The ash and water vapour from volcanic eruptions can also cause tropospheric anomalies [5]. In recent years, benefiting from the development of GNSS technique, the means of using GNSS to observe ionosphere, troposphere, and ground displacement have been continually improved and the accuracy of the observations has been increasing. Volcanic eruptions are usually accompanied by strong earthquakes, and the relationship between earthquakes and ionospheric anomalies has been studied since the 1965 Alaska earthquake in the USA. The discovery by Leonard and Barnes Jr [6] of ionospheric anomalous perturbations at the time of this major earthquake led to a wave of research on the correlation between the ionosphere and earthquakes. The scientists showed that anomalous changes in the ionosphere associated with seismic activity actually exist and concluded that lithosphere–atmosphere–ionosphere coupling excites disturbances in the ionosphere and atmosphere [7–9]. Numerous works have found that ionospheric anomalous perturbations do exist before and after earthquakes and have a conjugate structure with a tendency to drift towards the magnetic equator [10–12]. Studies of seismic ionospheric effects from Mw 6+ earthquakes located in the Pacific Rim seismic zone also show a strong correlation between total electron content (TEC) anomalies and magnitude, source depth, and geographic location [10,13].

Volcanic eruptions produce large amounts of water vapour and ash which can cause anomalies in GNSS signal delays. Solheim et al. [14] studied the relationship between atmospheric water vapour, water condensate, and other particles (sand, dust, aerosols, and volcanic ash) and GNSS signal propagation and concluded that the propagation delays of water vapour, cloud liquid, rain, and dust storms are closely related to GNSS precision positioning. Stoycheva et al. [15] studied the process of fog formation, development, and dissipation through GNSS. GPS data were also taken to analyze the relationship between haze and zenith delay, and the results showed that haze varies synchronously with zenith delay [16]. Tang et al. [17] researched typhoons using GPS technology which showed that GPS-estimated PWV changes could be used to predict whether a typhoon would land. Guo et al. [18,19] used GNSS to detect particulate matter from forest fires and found that the concentration of particulate matter had a high correlation with GNSS non-hydrostatic delay.

Volcanic eruptions are often accompanied by strong seismic activity, and anomalous disturbances may occur at ground-based GNSS station locations during both the preparation process of earthquakes and earthquake occurrences, making GNSS technique widely used in the detection of anomalous pre-seismic and co-seismic crustal deformation. Wallace et al. [20] studied the 2010–2011 slow slip event in the Hickory subduction zone of New Zealand and found that, unlike in other regions, one year after the long-term slow slip event in this region, short-term creep slip occurred, with the onset of this phenomenon occurring in the upper part of the plate interface locking region, which may be related to interseismic coupling. Socquet et al. [21] studied the precursory mechanism of the 2014 intellectual Mw8.1 earthquake and showed that GNSS stations in the coastal region accelerated westward eight months before the main earthquake. Chen et al. [22] explored the pre-seismic and co-seismic deformation field characteristics of the 2011 Mw9.0 earthquake in Japan and pointed out that the pre-seismic trend offset of GNSS coordinate time series is useful for earthquake precursor characterization. Yue et al. [23] used high-frequency GPS observations to invert the rupture process of the 9.0 magnitude earthquake in Japan and found anomalies in ground displacement before and after the earthquake.

Previous studies have analyzed the anomalies caused by volcanoes from a single aspect. The purpose of this paper is to comprehensively analyze the environmental anomalies caused by the 2022 Tonga volcano eruption from the ionosphere, troposphere, and station location based on GNSS technique. A new method combining the zenith non-hydrostatic delay difference (ΔZNHD) method and the ESMD method was proposed to detect tropospheric anomalies. The moving interquartile range (MIQR) method and the ESMD method

were introduced to detect ionospheric anomalous perturbations and coordinate time series anomalies respectively. Section 2 introduces data collection and research methods. Results and analysis are presented in Section 3. Finally, the conclusion is given in Section 4.

2. Materials and Methods

2.1. Materials

As the Tonga volcano is located in the Kingdom of Tonga, a South Pacific island nation, there is only one GNSS station available nearby, approximately 70 km from the eruption centre. Therefore, this station was chosen as an example. The GNSS coordinate time series were obtained from The Nevada Geodetic Laboratory (http://geodesy.unr.edu/index.php (accessed on 23 September 2022)), with a 5 min sampling interval and a coordinate time series period of 15 December 2021–15 February 2022. GNSS ZNHD time series are obtained from the Nevada Geodetic Laboratory (http://geodesy.unr.edu/index.php (accessed on 23 September 2022)), with a time resolution of 1 h.

The data processing strategy [24] is shown in Table 1.

Table 1. The data processing strategy.

Parameter	Strategy
Software used	GipsyX Version 1.0
Elevation angle cutoff	7°
Mapping function	Vienna Mapping Function (VMF1)
Estimated frequency of tropospheric parameters	Zenith delay and gradients as random walk every 5 min
Ionosphere corrected	1st order effect: Removed by LC and PC combinations 2nd order effect: Modeled using IONEX data with IGRF12
Solid earth tide and pole tide	IERS 2010 Conventions
Ocean tide loading	FES2004
Earth orientation parameter (EOP) model	IERS 2010 Conventions for diurnal, semidiurnal, and long period tidal effects on polar motion and UT1

In order to ensure the reliability of the experimental results, we analyzed the reliability of the data from the geological characteristics and data accuracy of the Tonga Station. The monument of the Tonga Station is made of concrete block and its geological characteristic is bedrock. Therefore, the geological characteristics are very stable. We have computed statistics on the calculation accuracy of the data of the Tonga Station for the period 15 December 2021–15 February 2022, as shown in Table 2. The mean of 5 min final coordinate solution accuracy in directions E, N, and U are 8.1 mm, 9.7 mm, and 25.8 mm, respectively. The accuracy of ZTD and PWV is 2.21 mm and 0.36 mm, respectively. The accuracy of ZNHD should be better than 2.21 mm. To sum up, the data of the Tonga Station is stable and reliable.

Table 2. Accuracy statistics of coordinate solution and tropospheric solution of the Tonga Station (mm).

Index		Max	Min	Mean	Std
Coordinate	E	22.3	5.5	8.1	2.1
	N	26.9	6.6	9.7	2.5
	U	55.1	20.8	25.8	7.9
Troposphere	ZTD	3.30	1.70	2.21	0.26
	PWV	0.53	0.28	0.36	0.04

To calculate the ZNHD due to water vapour, "total_column_water_vapour" data from the ERA5 model was also used, for the period 15 December 2021–15 February 2022. The temporal resolution of the data is 1 h. The spatial grid size is 0.25° × 0.25°.

The TEC data are derived from the Global Ionospheric Map (GIM) provided by the Centre for Orbit Determination in Europe (CODE) (ftp://ftp.unibe.ch/aiub (accessed on 23 September 2022)) from 18 December 2021 to 16 January 2022. The GIM data are obtained from IGS stations and national GPS stations at two-hour intervals forming a $5^\circ \times 2.5^\circ$ grid.

In order to exclude anomalous solar perturbations to the ionosphere, the solar radio flux F10.7 and sunspot number SSN (http://www.sepc.ac.cn (accessed on 23 September 2022)) provided by the Space Centre of the Chinese Academy of Sciences for the period from 18 December 2021 to 16 January 2022 were analyzed in this paper.

2.2. Methodology

2.2.1. Zenith Non-Hydrostatic Delay Difference Calculation Method

The zenith total delay (ZTD_G) was processed as an unknown parameter using the GNSS carrier phase observation equation [25].

$$L_{i,f}^j = \rho_i^j + c\left(dt_i - dt^j\right) + M * ZTD_G - I_{i,f}^j + \lambda_f N_{i,f}^j + \varepsilon_{i,f}^j \quad (1)$$

where i is the receiver, j is the satellite, ρ_i^j is the geometric distance from the receiver to the satellite, c is the speed of light, dt_i is the receiver clock offset, dt^j is the satellite clock offset, M is the troposphere mapping function, $I_{i,f}^j$ is the slant ionosphere delay, λ_f is the wavelength of phase observation, $N_{i,f}^j$ is the phase ambiguity, $\varepsilon_{i,f}^j$ is other errors. The zenith hydrostatic delay (ZHD_G) was then calculated using the Saastamoinen model [26].

$$ZHD_G = \frac{0.00227768 * P}{1 - 0.00266 * COS(2L) - 0.00028 * H} \quad (2)$$

where P is the atmospheric pressure, L is the latitude of the GNSS station, and H is the height of the GNSS station. The ZTD_G minus the $ZNHD_G$ gives the GNSS calculated tropospheric non-hydrostatic delay ($ZNHD_G$), and the equation is

$$ZNHD_G = ZTD_G - ZHD_G \quad (3)$$

The delay in the atmosphere caused by liquid water and water vapour is given by [27]

$$ZNHD_V = \frac{\beta'_{vap}}{T_{eff}} \int_0^R \rho_{vap}(z) dz \quad (4)$$

where $\rho_{vap}(z)$ is the water vapour density at height Z and R is the maximum height of the integral, usually considered to be the top of the water vapour, i.e., the total column water vapour, which can be obtained with the ERA5 model. The mid-latitudes are based on empirical values that take $\frac{\beta'_{vap}}{T_{eff}} = 6.19\ \left(\mathrm{cm^3 g^{-1}}\right)$, where $\beta'_{vap} = 1720.6^\circ\ \left(\mathrm{Kcm^3 g^{-1}}\right)$ and $T_{eff} = 278^\circ \mathrm{K}$.

The ZTD_G is the delay caused by all substances in the atmosphere, which includes delays caused by substances such as standard dry atmosphere, water vapour, and particulate matter. The ZHD_G is the delay caused by the standard dry atmosphere calculated by the model, which does not include delays caused by substances such as particulate matter in the atmosphere. Therefore, the delay caused by substances such as particulate matter in the air can be expressed as

$$\Delta ZNHD = ZNHD_G - ZNHD_V \quad (5)$$

where $\Delta ZNHD$ is the zenith non-hydrostatic delay difference.

2.2.2. Extreme-Point Symmetric Mode Decomposition Method

The ESMD method is an improvement and innovation of the empirical mode decomposition (EMD) method [28,29]. The ESMD method is able to smooth complex signals so that the different scales or periodic oscillations and trend components inherent in the original signal sequence are extracted step by step, resulting in a number of eigenmodes (Models) with different characteristic scales or intrinsic periods, as well as the true trend components. The ESMD is one of the latest methods for extracting signal trends, as it effectively solves the "modal conflation" (or "frequency crossover") problem in the decomposition of EMD methods [28,29]. Due to its adaptive and local variability-based nature, the ESMD method is widely applicable to the processing and analysis of non-stationary, non-linear signals (data) in the fields of oceanography, atmospheric science, ecology, and seismology [29]. The ESMD modal decomposition process is as follows:

(1) Enter the time series $Y(t)$, set the maximum number of filters, find all the poles in the time series and denote them as $E_i(1 \le i \le n)$, connect the adjacent poles with a line segment, denote the midpoint of the line segment as $F_i(1 \le i \le n-1)$ in turn, and add the left and right boundary midpoints F_0 and F_n. The boundary midpoints are supplemented as follows:

Linear interpolation is conducted using the 1st and 2nd extreme value points, and then linear interpolation is conducted using the 1st and 2nd extreme value points to obtain two interpolation lines noted as $Y(t) = k_1 + b_1$ and $Y(t) = k_2 + b_2$, respectively; the 1st point of the data is then noted as Y_1, and the boundary midpoints are then supplemented according to the following three scenarios:

a. If $b_2 \le Y_1 \le b_1$, define b_1 and b_2 as the boundary maxima and minima, respectively.
b. If $b_1 \le Y_1 \le (3b_1 - b_2)/2$ (or $(3b_1 - b_2)/2 \le Y_1 \le b_2$), then define Y_1 and b_2 (or b_1 and Y_1) as the boundary maxima and minima, respectively.
c. If $Y_1 > (3b_1 - b_2)/2$ (or $(3b_1 - b_2)/2 > Y_1$), then define Y_1 as the boundary minima (or minima) and use the line leading from the first minima to define the boundary minima (or minima). The magnitude of the slope here is determined by the left boundary point) and the line at the first extreme value point.

(2) Two interpolation curves, denoted L_1 and L_2, are constructed from the obtained $n+1$ midpoints, the midpoints of odd order L_1 are generated by cubic spline interpolation, and the midpoints of even order L_2 are generated by cubic spline interpolation to calculate the mean curve L^*:

$$L^* = (L_1 + L_2)/2 \tag{6}$$

(3) Repeat steps (1) and (2) for the sequence $Y(t) - L^*$ until $|L^*| \le \varepsilon$ or the set maximum number of screens is reached, at which point the decomposition yields the first empirical mode *Model* 1, where ε is a predetermined allowable error usually taken as $0.0001\sigma_0$ and σ_0 can be expressed as

$$\sigma_0^2 = \frac{1}{N}\sum_{i=1}^{N}\left(y_i - \overline{Y}\right)^2 \tag{7}$$

where $\overline{Y}$ is the global average.

(4) Repeat steps (1)–(3) for the $Y(t) - Model\ 1$ sequence to obtain *Model* 2, *Model* 3, ... in turn until the trend residual term $R(t)$ matches the predetermined number of remaining poles l.

(5) Given that the maximum number of screening K takes values within the integer interval $[K_{min}, K_{max}]$, calculate the variance ratio G. Note that the time series is $Y(t) = \{x_i\}_{t=1}^{N}$, the trend term is $R(t) = \{r_i\}_{t=1}^{N}$, and the variance ratio G can be expressed as

$$G = \frac{\sigma}{\sigma_0} \tag{8}$$

$$\sigma = \frac{1}{N}\sum_{i=1}^{N}(y_i - r_i)^2 \quad (9)$$

When G is smallest, it means that the time series with the trend term $R(t)$ removed is closest to the original time series $Y(t)$, i.e., the decomposition works best.

(6) Determine the minimum variance ratio corresponding to the number of times to execute a large screening K_0, at which point $R(t)$ is the best-fit curve, then repeat steps 1–5 at K_0 to obtain the best decomposition result.

3. Results and Discussion

3.1. Analysis of Ionospheric Anomalies Prior to the Tonga Volcanic Eruption

The release of large amounts of energy from the crust during volcanic eruptions can cause anomalies in the ground position and also affect the ionosphere and upper atmosphere [5]. Therefore, the study of ionospheric anomalies before volcanic eruptions is important for further research on the dynamic coupling mechanism between the lithosphere and the atmosphere before volcanic activity [9,30].

(1) Anomalous TEC disturbance detection prior to the Tonga volcanic eruption

The closest GNSS TEC to the HTHH underwater volcano eruption site in Tonga was extracted from the GIM information provided by CODE. We compared bilinear interpolation, cubic spline interpolation, and nearest neighbor interpolation algorithms through experiments; we found that the accuracy of bilinear interpolation and cubic spline interpolation is similar, but the efficiency of bilinear interpolation is the highest, and the accuracy of nearest neighbor interpolation is poor. Therefore, the bilinear interpolation was used to obtain the TEC at the eruption center. Using the MIQR, a 27-day ionospheric anomaly at the center of the HTHH underwater volcano eruption was detected using the observations at the same time on 27 days as the background value and 1.5 times the interquartile range as the limit difference. The results are shown in Figure 1.

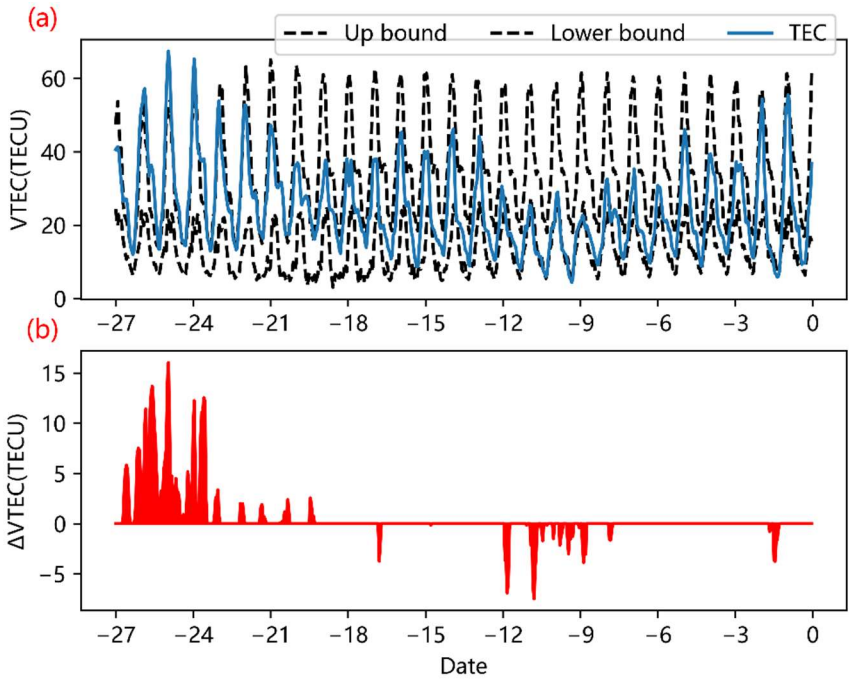

Figure 1. Results of ionospheric anomaly detection near the eruption centre of the HTHH underwater volcano (0 represents the day of the eruption). (**a**) Variation in TEC, upper TEC limit, and lower TEC limit (**b**) Time distribution of TEC anomaly value.

As can be seen in Figure 1, TEC levels were high on the 27th day before the eruption, exceeding 60 TECU, gradually decreasing from the first 24 days, reaching a minimum TEC

level of below 30 TECU from the first 11 days to the first 8 days, and then gradually starting to increase again, exceeding 55 TECU on the day of the eruption.

For most of the 27 days before the volcanic eruption, the TEC in the HTHH underwater volcano eruption center was within the normal range, but some abnormal moments were still detected. Large-scale positive TEC anomalies were observed from day 22 to day 27 before the HTHH eruption, with anomalies exceeding 10 TECU at some moments. Minor negative anomalies were observed on day 16, day 10, and day 1 before the HTHH eruption, all with anomalies less than 5 TECU.

In order to exclude TEC anomalies partially caused by solar activity, we also analyzed the solar radio flux F10.7 and sunspot number (SSN) for the 27 days before the HTHH volcano eruption; anomaly detection was also performed using the MIQR method, and the results are shown in Figure 2.

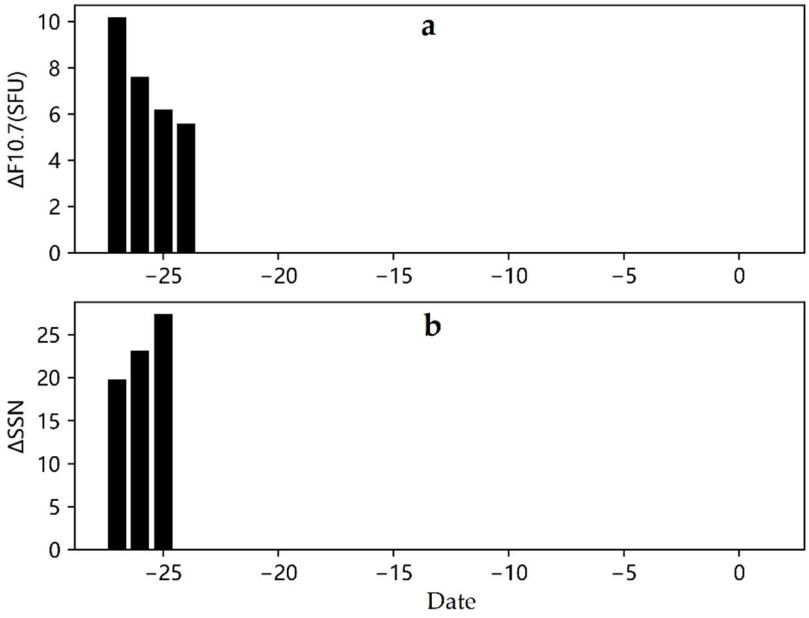

Figure 2. Solar activity anomaly detection results (0 represents the day of the eruption). (**a**) Represents the anomaly detection result of the solar radio flux F10.7, and (**b**) represents the anomaly detection result of sunspot number (SSN).

As can be seen from Figure 2, the solar activity was generally stable during the nearly one-month period before the HTHH eruption, but some periods of anomalies still occurred. As shown in Figure 3a, significant anomalies were observed on day 26 and day 27 before the HTHH volcano eruption, with anomalous values reaching 6 SFU and 1 SFU, respectively. As shown in Figure 2b, the SSN index was also accompanied by significant anomalies on days 25, 26, and 27 before the HTHH volcano eruption, with anomalous values exceeding 7. Combined with the TEC anomaly results in Figure 2, it is clear that the TEC anomaly 27–25 days before the HTHH underwater volcano eruption may have been caused by solar activity.

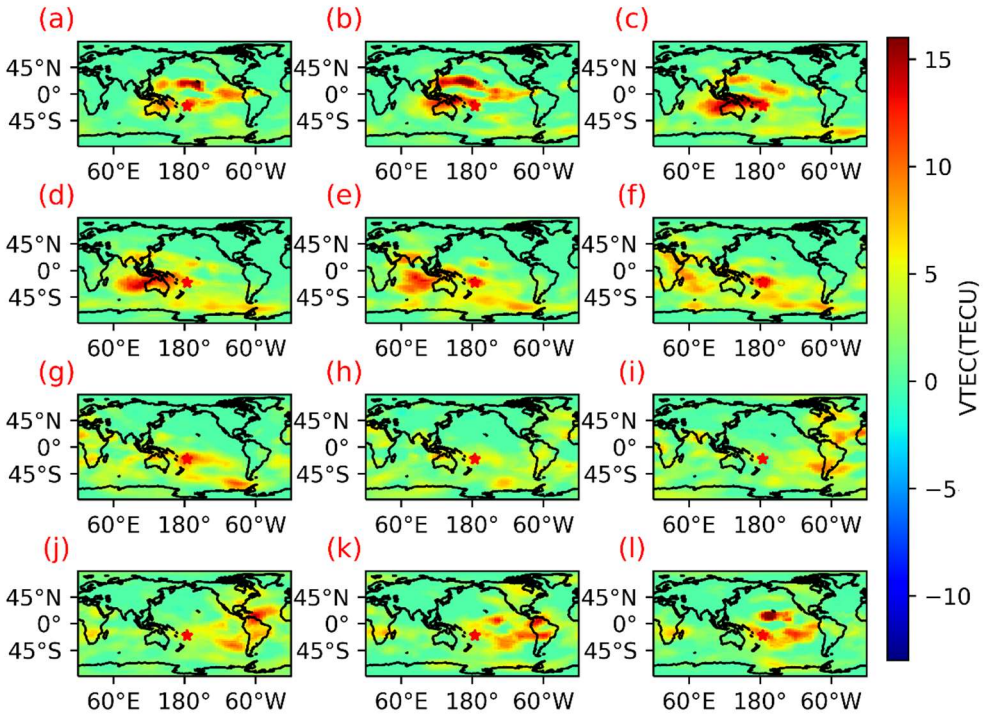

Figure 3. Global TEC anomaly distribution for 24th day prior to the HTHH volcano eruption. (**a**–**l**) are 0:00–24:00 UTC, respectively, at 2 h intervals; the position of the pentagram is the location of the eruption center.

(2) Global distribution of TEC anomalous disturbances

According to the results of TEC abnormal disturbance detection in the HTHH underwater volcano eruption center, the TEC abnormal disturbance 22 to 27 days before the HTHH underwater volcano eruption is particularly obvious. At the same time, considering the detection results of solar activity anomalies, we studied the global TEC anomaly distribution on the 24th day before the HTHH underwater volcano eruption. The global TEC anomaly distribution on the day of the HTHH underwater volcano eruption and the day before was also analyzed.

It can be seen from the figure that at 0:00 on the 24th day before the HTHH underwater volcano eruption, a wide range of TEC anomalies appeared in the HTHH underwater volcano eruption center, the north, east, and west of the center. At 2:00, the intensity and range of TEC anomaly further increased, and the maximum anomaly reached 16TECU. At 4:00, the TEC anomaly on the north side of the HTHH underwater volcano eruption center gradually decreased, and the TEC anomaly range and intensity on the west side of the HTHH underwater volcano eruption center and the west side further increased. At 6:00–10:00, there was still a large area of TEC anomaly in and around the HTHH underwater volcano eruption center, but the anomaly intensity decreased gradually. At 12:00–14:00, the range and intensity of TEC anomalies gradually decreased. At 16:00–22:00, TEC anomalies in the HTHH underwater volcano eruption center, northwest, and east of the center tended to increase. However, it can be seen from Figures 2 and 3 that during the 22–27 days before the volcanic eruption, F10.7, SSN, and TEC had obvious abnormal phenomena, and the trend of abnormal changes was similar. Therefore, we believe that the TEC anomaly during the 22–27 days before the eruption of the volcano was caused by solar activity and had little to do with the eruption of the HTHH underwater volcano.

Figures 4 and 5 show the global TEC anomaly distribution on the day of the HTHH underwater volcano eruption (15 January 2022) and the day before. The HTHH underwater volcano erupted at approximately 5:30–6:00 UTC. As can be seen in Figures 4 and 5, approximately 9–10 h before the HTHH underwater volcano eruption, large TEC anomaly disturbances were observed to the northwest and southwest of the HTHH underwater vol-

cano eruption center, with particularly strong anomalies in the northwest, with anomalies' maximum exceeding 15 TECU, and a significant negative anomaly near the south pole. At 2:00 UTC, the TEC anomaly was mainly distributed due north and west of the eruption center, with a marked decrease in extent and intensity of the anomaly. At 6:00 UTC, the extent and intensity of the TEC anomaly were further reduced. As time progressed, the TEC anomaly gradually moved from west to east and its extent diminished, and by 18:00 UTC, the global ionosphere returned to calm.

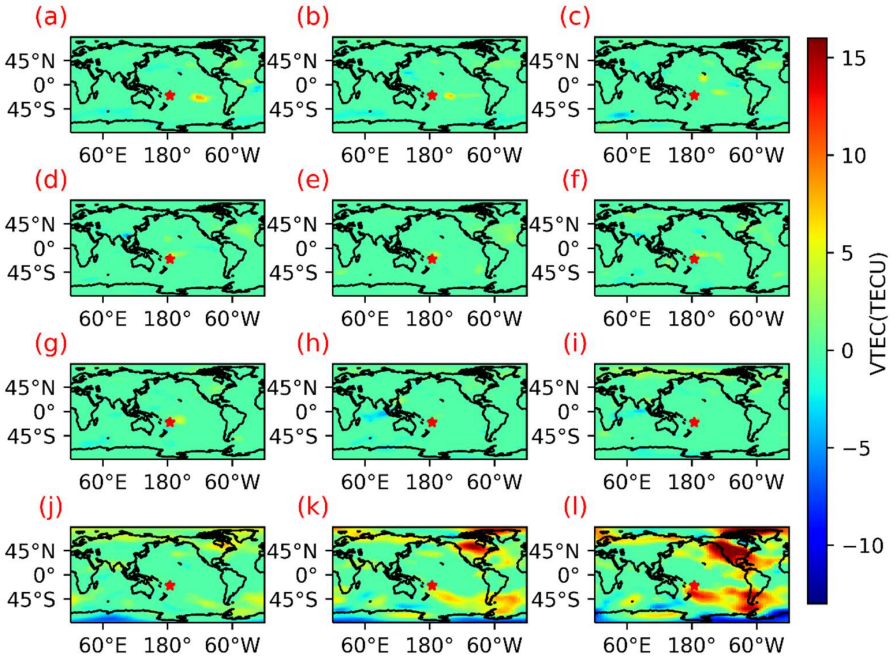

Figure 4. Global TEC anomaly distribution the day (2022/1/14) before HTHH volcanic eruption. (**a**–**l**) are 0:00–24:00 UTC, respectively, at 2 h intervals; the position of the pentagram is the location of the eruption center.

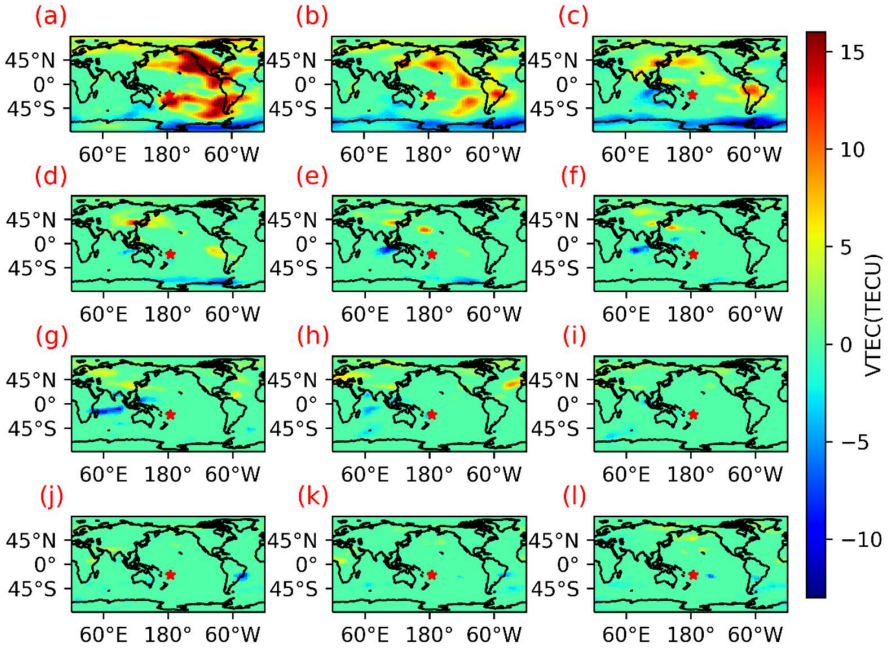

Figure 5. Global TEC anomaly distribution on the day (2022/1/15) of the HTHH volcanic eruption. (**a**–**l**) are 0:00–24:00 UTC, respectively, at 2 h intervals; the position of the pentagram is the location of the eruption center.

3.2. Analysis of Tropospheric Anomalies before and after the Tonga Volcanic Eruption

As the HTHH volcano is a submarine volcano, the scale of this eruption is huge, and the eruption produced a large amount of volcanic ash and water vapour. Therefore, it may have had a great impact on the tropospheric delay of GNSS signal. The tropospheric delay calculated by GNSS is divided into ZHD_G (also known as zenith dry delay) and $ZNHD_G$ (also known as zenith wet delay). The ZHD_G is calculated from the standard atmospheric composition, while the $ZNHD_G$ is calculated using the ZTD_G minus the ZHD_G. Delays caused by substances in the atmosphere other than the standard atmosphere (e.g., volcanic ash, water vapour, etc.) are included in the $ZNHD_G$. In contrast, the $ZNHD_V$ calculated from meteorological parameters is due to water vapour only. Therefore, the difference between the $ZNHD_G$ and $ZNHD_V$ is caused by substances other than water vapour, including atmospheric particulate matter, etc. In this paper, the $ZNHD$ and the $\Delta ZNHD$ were used as the subject of this study, and the ESMD method was introduced to analyze the anomalies over the troposphere before and after the HTHH eruption.

First, the $ZNHD_G$, the $ZNHD_V$, and $\Delta ZNHD$ from 1 December 2021–31 January 2022 were studied and the results are shown in Figure 6.

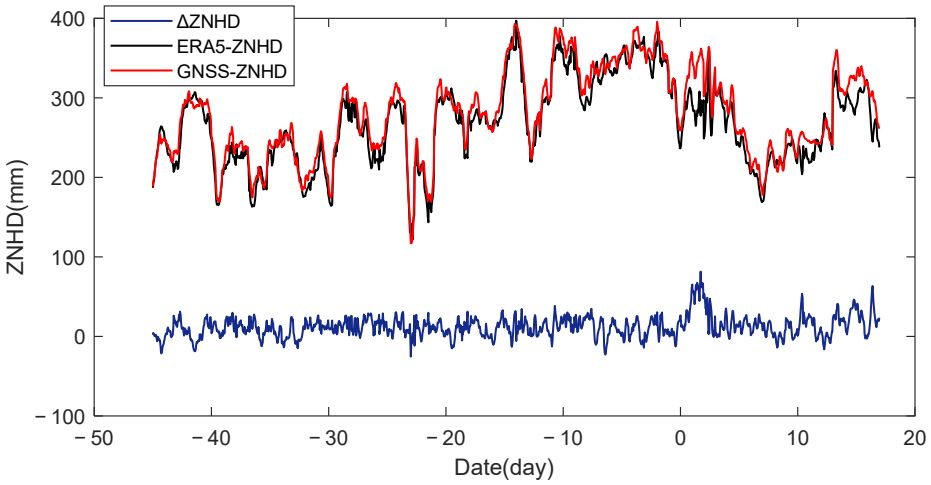

Figure 6. Variation in zenith non-hydrostatic delay (0 represents the day of the eruption).

As can be seen from Figure 6, the $ZNHD_G$ and $ZNHD_V$ are in very high agreement. Statistically, the correlation between the $ZNHD_G$ and $ZNHD_V$ before the HTHH underwater volcano eruption (before 15 January 2022) is as high as 93.76%. After 15 January, the agreement between them begins to decline, with their correlation dropping to 88.23%. It is also clear from the $\Delta ZNHD$ that most of the $\Delta ZNHD$ was below 30 mm and varied relatively smoothly until 15 January. Between 15 and 16 January, the $\Delta ZNHD$ increased significantly, with a maximum of over 80 mm, and the subsequent fluctuations also increased significantly. The above phenomenon indicates that the HTHH underwater volcano eruption had a relatively large impact on the GNSS tropospheric observations.

To further analyze the impact of the HTHH underwater volcano eruption on GNSS tropospheric observations, the two-month ΔZNHD time series was decomposed using the ESMD method. The time-varying frequency and amplitude of the decomposed signal (Model) were analyzed. The results are shown in Figure 7.

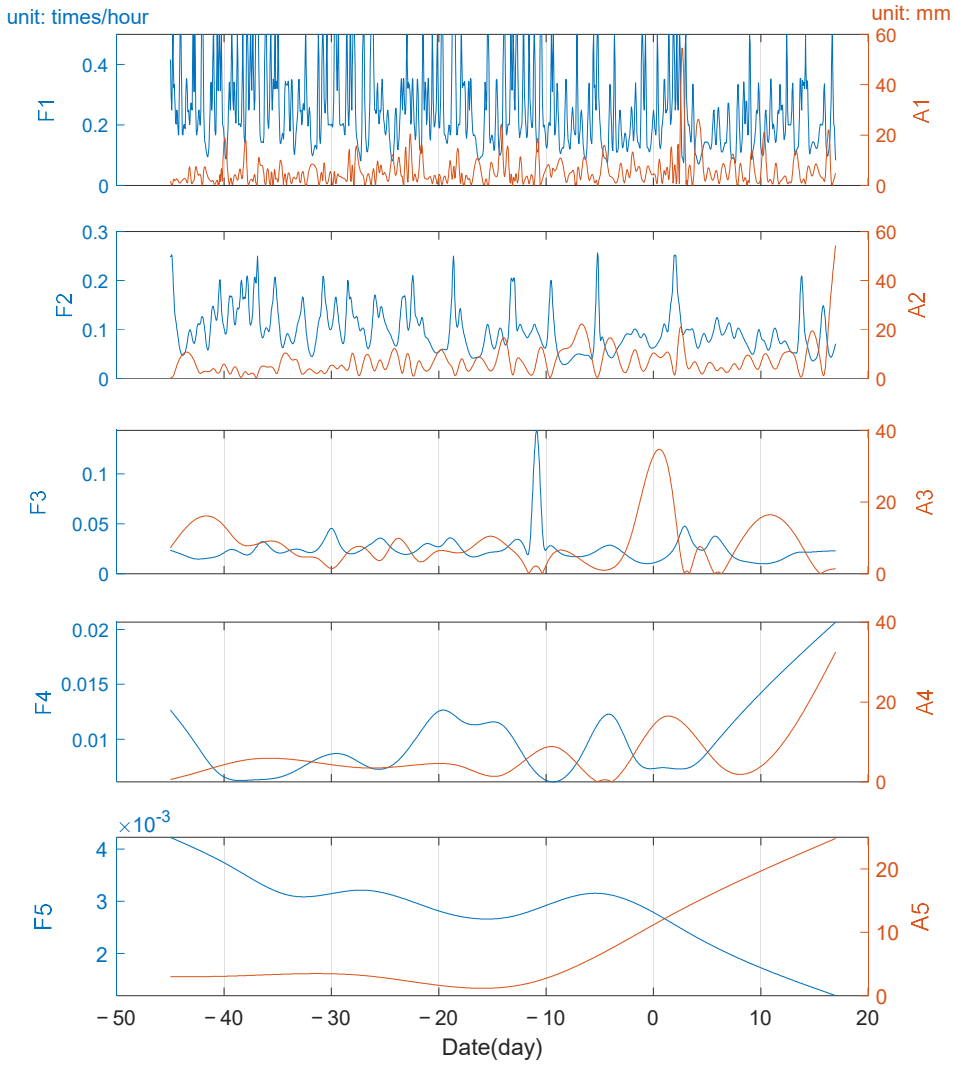

Figure 7. Time-varying amplitude (A1–A5) and frequency (F1–F5) of different model signals of $\Delta ZNHD$ (0 represents the day of the eruption).

As can be seen from Figure 7, the amplitude of the Model 1 signal increased significantly 1–3 days after the HTHH underwater volcano eruption, with the anomalous amplitude being approximately 3–4 times the normal level, and the frequency of the signal also remains at a low level 3–4 days after the HTHH underwater volcano eruption. The Model 2 signal showed a significant reduction in high-frequency signal after the HTHH underwater volcano eruption, and the amplitude of the Model 3 signal showed a significant anomaly on the day of the HTHH underwater volcano eruption, with anomalies up to three times the normal size. Similarly, the amplitude of the Model 4 signal showed a significant anomaly on the day of the HTHH underwater volcano eruption.

In addition, the total energy of the $\Delta ZNHD$ signal was analyzed, as shown in Figure 8. The equation of total energy is

$$E(t) = \frac{1}{2}\sum_{j=1}^{n} A_j^2(t) \tag{10}$$

where A is the amplitude of the jth Mode.

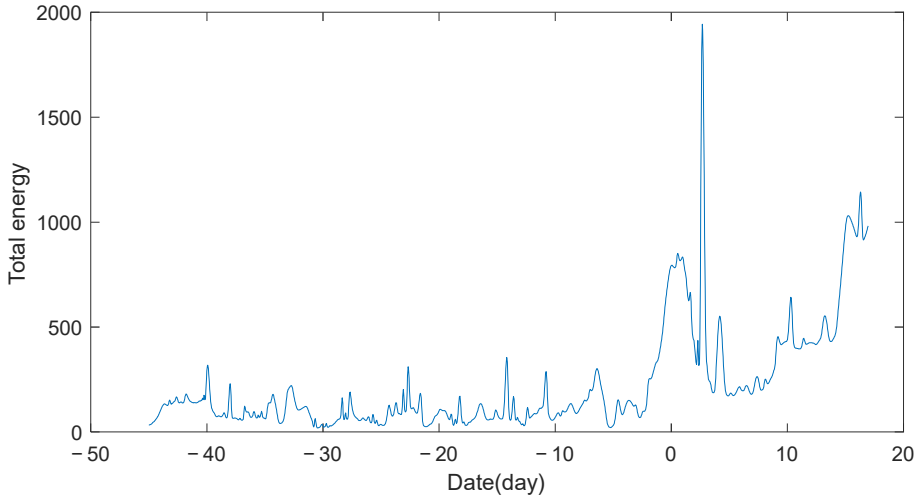

Figure 8. Total energy distribution of the ΔZNHD time series (0 represents the day of the eruption).

On the day of the HTHH underwater volcano eruption, the total signal energy increased significantly, and was approximately three times that of the energy before the volcanic eruption. The most pronounced anomalies appeared 2–3 days after the eruption, with anomaly sizes reaching more than 10 times that of the energy before the HTHH underwater volcano eruption, and the signal energy has remained high since the HTHH underwater volcano eruption.

3.3. Influence of the HTHH Underwater Volcano Eruption on the Location of GNSS Station

The HTHH underwater volcano eruption was accompanied by strong seismic activity, and the occurrence of earthquakes can have a significant impact on GNSS station locations. In addition, GNSS stations may also have a certain response during the earthquake preparation period and a period of time after the earthquake. Therefore, high-frequency coordinate time series (one solution every 5 min) for one month before and one month after the HTHH underwater volcano eruption were analyzed using the ESMD method. The coordinate time series in the directions N, E, and U were decomposed to analyze the amplitude and frequency characteristics of each decomposed signal (Model), and the results were shown in Figures 9–11.

As can be seen from Figure 9, the Model 1 signal amplitude of GNSS coordinate time series in direction E had obvious abnormal disturbance before and after the HTHH underwater volcano eruption. The first disturbance before the HTHH underwater volcano eruption occurred at approximately 2:45 p.m. on 14 January, and the abnormal amplitude reached 0.062 m, approximately 2–3 times that of the daily amplitude. From 4:30 a.m. to 5:40 a.m. on 15 January, the abnormal amplitude was approximately 0.093 m, reaching 4–5 times that of the daily amplitude. At approximately 3:45 a.m. on 16 January, the abnormal amplitude was approximately 0.073 m. The Model 2 signal disturbance occurred at the same time as the Model 1 signal disturbance. However, the extent of the disturbance was smaller, with anomalous amplitudes of 0.051 m, 0.062 m, and 0.036 m, respectively. The Model 3–Model 7 signal anomalous disturbances were not significant. The frequency of Model 8 and Model 9 signals increased significantly on the 10th day after the earthquake. The decomposition results in Figure 10 show that the anomalous response of coordinate time series at direction N to the HTHH underwater volcano eruption was not significant. From the results in Figure 11, during the HTHH underwater volcano eruption, Model 1–Model 3 signals had obvious amplitude abnormal disturbance, and the amplitude abnormal sizes were 0.37 m, 0.21 m, and 0.16 m, respectively.

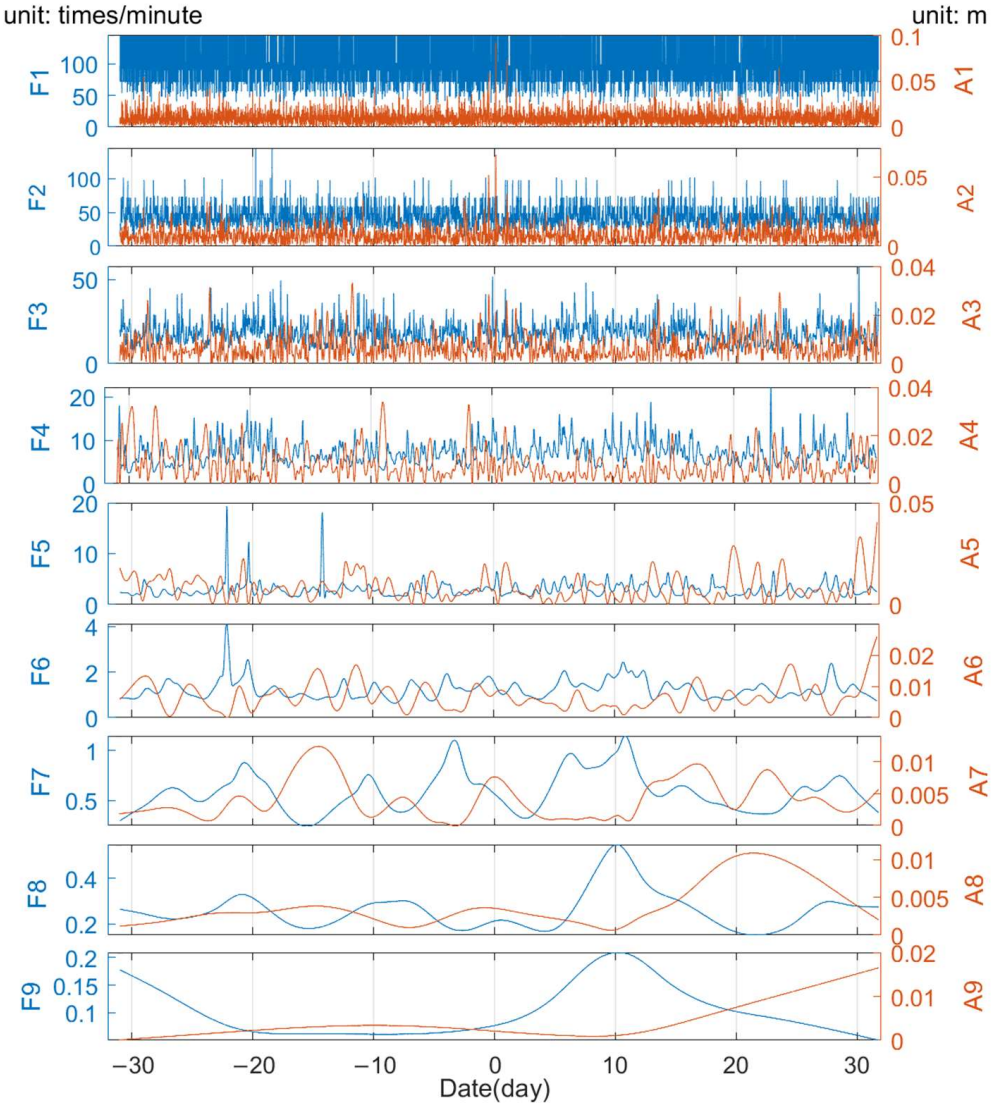

Figure 9. Time-varying amplitudes and frequencies of different Model signals for direction E coordinate time series (0 represents the day of the eruption).

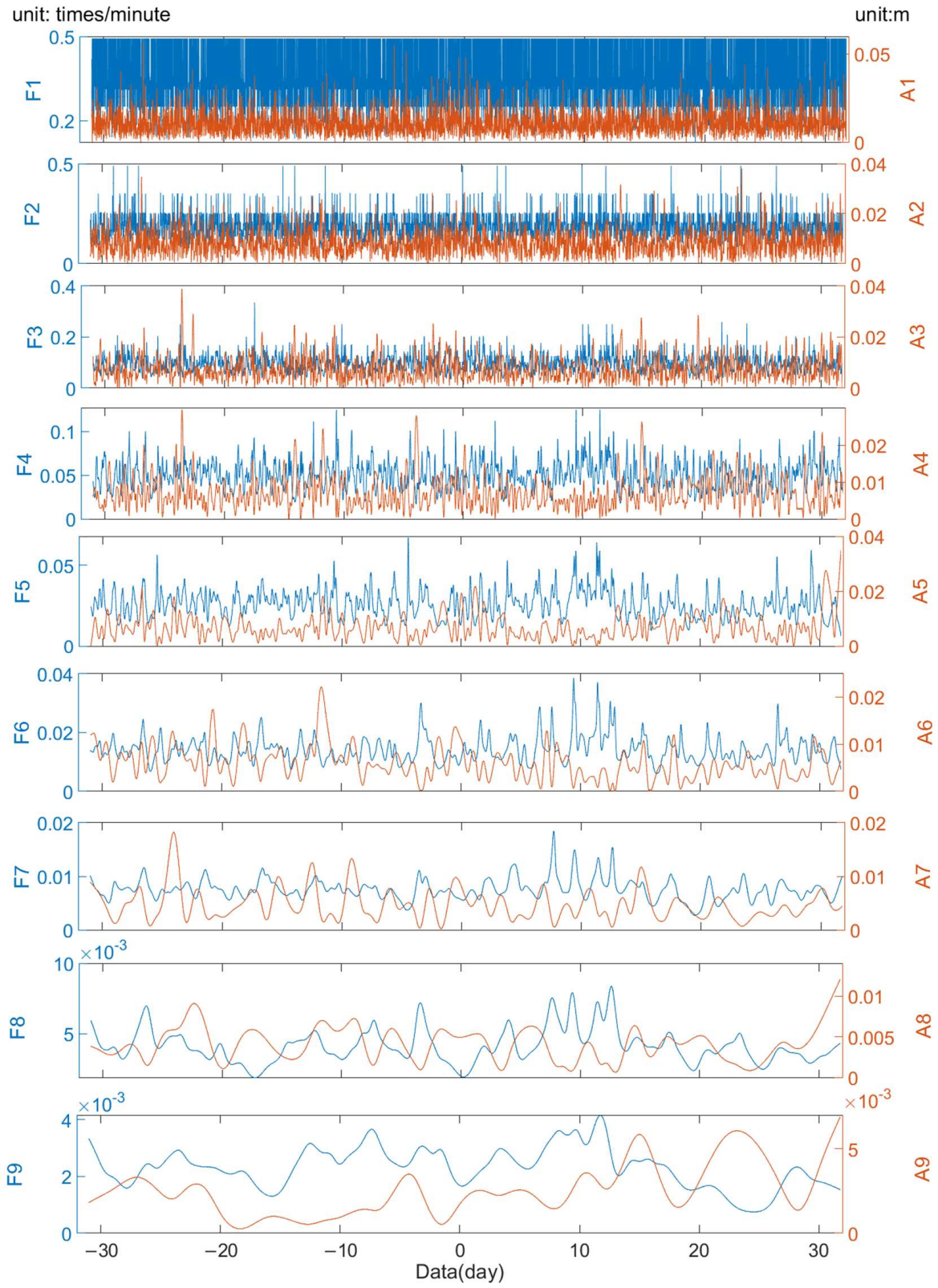

Figure 10. Time-varying amplitudes and frequencies of different Model signals for direction N coordinate time series (0 represents the day of the eruption).

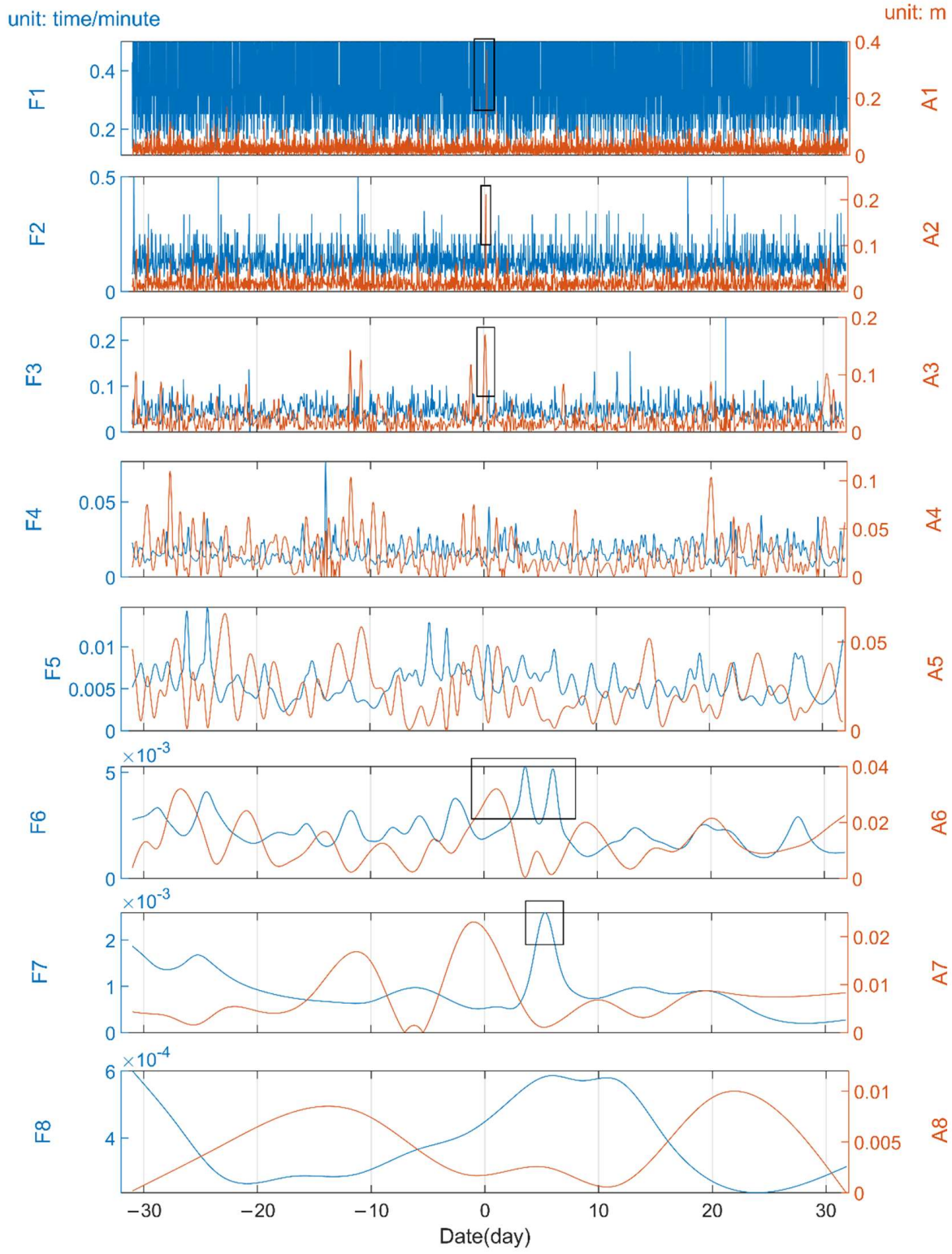

Figure 11. Time-varying amplitudes and frequencies of different Model signals for direction U coordinate time series (0 represents the day of the eruption).

The total energy of the signal has also been analyzed and the results are shown in Figure 12.

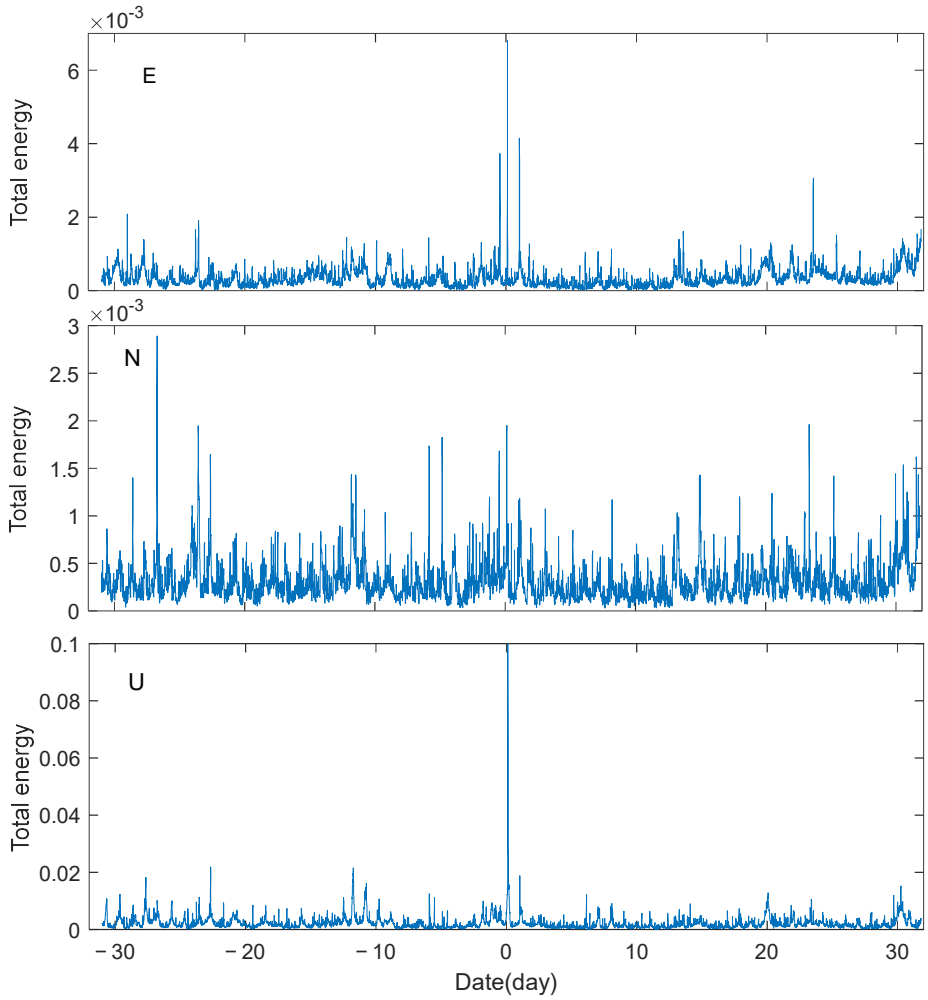

Figure 12. Total energy distribution of the coordinate time series (0 represents the day of the eruption).

It can be seen from Figure 12 that there are very obvious energy abnormalities in direction E at approximately 2:45 p.m. on 14 January, 4:30–5:40 a.m. on 15 January, and 3:45 a.m. on 16 January. The three obvious abnormalities reach 3–4 times, 7–8 times, and 4–5 times that of the daily level, respectively. The energy anomaly in direction N was not obvious. During the HTHH underwater volcano eruption, a very prominent energy anomaly can be observed in the direction U. The anomaly occurs from 4:30 a.m. to 5:40 a.m., and the intensity of the anomaly was more than 10 times that of the normal level.

In order to study the response mechanism of coordinate time series in different directions to the volcanic eruption, the plate tectonics near HTHH underwater volcano was studied, as shown in Figure 13. As can be seen from Figure 13, HTHH underwater volcano is located at the junction of the Australian plate and the Pacific plate, and the crustal movement is very active. The subduction of the Pacific plate under the Australian plate caused the Australian plate to rise upward, which accelerated the eruption of the HTHH underwater volcano. The relative motion of the Pacific plate and the Australian plate is mainly in the east–west direction and vertical direction. This also leads to more obvious abnormal responses of coordinate time series in direction E and direction U to HTHH underwater volcano eruption.

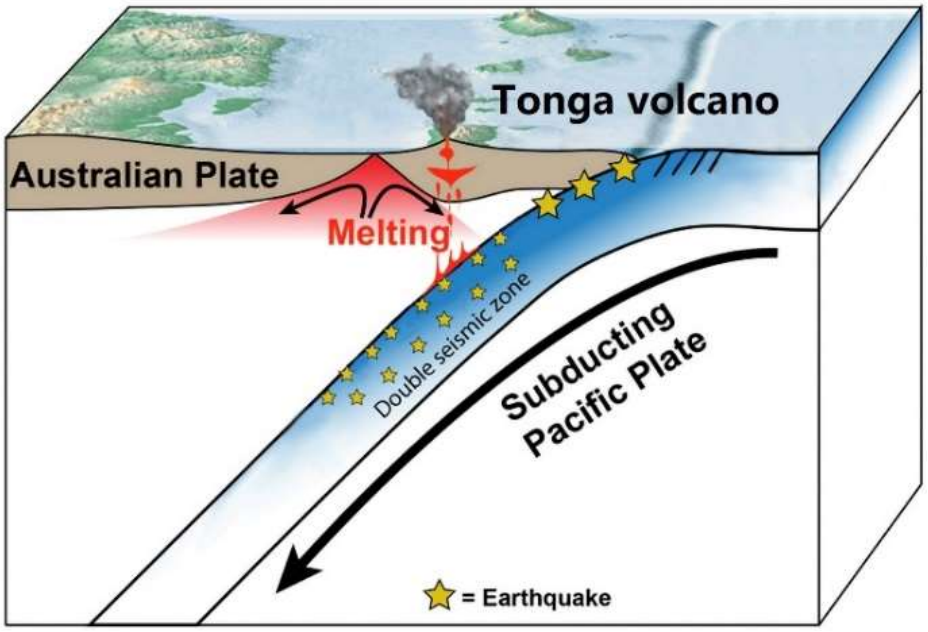

Figure 13. Plate tectonics near HTHH volcano.

4. Conclusions

In this paper, the method of combining ESMD and $\Delta ZNHD$ is proposed to detect the tropospheric anomaly caused by the HTHH underwater volcano eruption, and ESMD and MIQR method are introduced to detect the TEC anomaly and station position change anomaly caused by HTHH underwater volcano eruption. The following conclusions are drawn:

(1) Based on GNSS ionospheric data, F10.7, and SSN and using the moving interquartile range method, ionospheric anomalies were detected for 27 days prior to the HTHH underwater volcano eruption. The results show that the TEC shows large scale positive anomalies on days 22–27 before the eruption, with anomalies exceeding 10 TECU at some moments. However, we believe that the TEC anomaly during the 22–27 days before the eruption of the volcano was caused by solar activity. Minor negative anomalies, all less than 5 TECU, were observed on day 16, day 10, and day 1 before the HTHH underwater volcano eruption, with the TEC anomalies on days 25–27 before the eruption likely due to solar activity.

(2) Tropospheric anomalies were detected 45 days before and 15 days after the HTHH underwater volcano eruption based on $\Delta ZNHD$ and using the ESMD method. The results show significant tropospheric anomalies on the day of the HTHH underwater volcano eruption, 1–3 days after the eruption, and 16–17 days after the HTHH underwater volcano eruption, with maximum anomalies up to 10 times the normal level. The different responses of the three directions to anomalies were caused mainly by plate tectonics.

(3) Station location anomalies were detected based on GNSS high-frequency coordinate time series and using the ESMD method for one month before and one month after the HTHH underwater volcano eruption. The results show that direction E showed very significant anomalies at approximately 2:45 p.m. on 14 January, 15 January at approximately 4:30 a.m.–5:40 a.m., and at approximately 3:45 a.m. on 16 January, with anomalies reaching a maximum of 7–8 times the daily level. The anomaly in direction N is not obvious. Very prominent anomalies can be observed in the direction U from 4:30 to 5:40 a.m., and the intensity of the anomaly was more than 10 times that of the normal level.

Author Contributions: M.Z.: validation, writing—reviewing and editing, and investigation; H.G.: supervision and methodology; D.Y.: supervision and funding acquisition; J.G.: conceptualization and methodology; L.Z.: data curation and software; L.Y.: software and validation; and S.P.: supervision. All authors have read and agreed to the published version of the manuscript.

Funding: This research was funded by, the National Natural Science Foundation of China, grant number 42106172, the Natural Science Foundation of Shandong Province, grant number ZR2021QD135, the Key Research and Development Program of Shandong, grant number 2019GHY112017, State Key Laboratory of Tropical Oceanography, South China Institute of Oceanology, Chinese Academy of Sciences, grant number LTO2017, the Foundation of Institute of Oceanographic Instrumentation, Shandong Academy of Sciences, grant number HYPY202107, University-Industry Collaborative Education Program, grant numbers 202102245036 and 202101044002, the Project plan of pilot project of integration of science, education and industry, grant number 2022GH004 and 2022PY041, and in part by the Open Research Fund of State Key Laboratory of Estuarine and Coastal Research under Project SKLEC-KF202001.

Data Availability Statement: The GNSS coordinate time series and GNSS ZNHD time series were obtained from The Nevada Geodetic Laboratory (http://geodesy.unr.edu/index.php (accessed on 23 September 2022)). The TEC data were derived from the Global Ionospheric Map (GIM) provided by the Centre for Orbit Determination in Europe (CODE) (ftp://ftp.unibe.ch/aiub (accessed on 23 September 2022)). The solar radio flux F10.7 and sunspot number (SSN) (http://www.sepc.ac.cn (accessed on 23 September 2022)) were provided by the Space Centre of Chinese Academy of Sciences.

Conflicts of Interest: The authors declare no conflicts interest.

References

1. Themens, D.R.; Watson, C.; Žagar, N.; Vasylkevych, S.; Elvidge, S.; McCaffrey, A.; Prikryl, P.; Reid, B.; Wood, A.; Jayachandran, P.T. Global propagation of ionospheric disturbances associated with the 2022 Tonga volcanic eruption. *Geophys. Res. Lett.* **2022**, *49*, e2022GL098158. [CrossRef]
2. Zhang, S.-R.; Vierinen, J.; Aa, E.; Goncharenko, L.P.; Erickson, P.J.; Rideout, W.; Coster, A.J.; Spicher, A. 2022 Tonga volcanic eruption induced global propagation of ionospheric disturbances via Lamb waves. *Front. Astron. Space Sci.* **2022**, *9*, 871275. [CrossRef]
3. Klein, A. Volcano Eruption in Tonga Was a Once-in-a-Millennium Event. Available online: https://www.newscientist.com/article/2304822-volcano-eruption-in-tonga-was-a-once-in-a-millennium-event (accessed on 17 January 2022).
4. Arculus, R. Deeply explosive. *Nat. Geosci.* **2011**, *4*, 737–738. [CrossRef]
5. Pulinets, S.; Boyarchuk, K. *Ionospheric Precursors of Earthquakes*; Springer: Berlin, Germany, 2005.
6. Leonard, R.; Barnes, R. Observation of ionospheric disturbances following the Alaska earthquake. *J. Geophys. Res.* **1965**, *70*, 1250–1253. [CrossRef]
7. Sorokin, V.; Chmyrev, V.; Yaschenko, A. Electrodynamic model of the lower atmosphere and the ionosphere coupling. *J. Atmos. Sol. Terr. Phys.* **2001**, *63*, 1681–1691. [CrossRef]
8. Hayakawa, M.; Molchanov, O.; Team, N. Achievements of NASDA's earthquake remote sensing frontier project. *Terr. Atmos. Ocean. Sci.* **2004**, *15*, 311–327. [CrossRef]
9. Guo, J.; Li, W.; Yu, H.; Liu, Z.; Kong, Q. Impending ionospheric anomaly preceding the Iquique MW 8.2 earthquake in Chile on 2014 April 1. *Geophys. J. Int.* **2015**, *203*, 1461–1470. [CrossRef]
10. Li, W.; Yue, J.; Guo, J.; Yang, Y.; Zou, B.; Shen, Y.; Zhang, K. Statistical seismo-ionospheric precursors of M7. 0+ earthquakes in Circum-Pacific seismic belt by GPS TEC measurements. *Adv. Space Res.* **2018**, *61*, 1206–1219. [CrossRef]
11. Guo, J.; Shi, K.; Liu, X.; Sun, Y.; Li, W.; Kong, Q. Singular spectrum analysis of ionospheric anomalies preceding great earthquakes: Case studies of Kaikoura and Fukushima earthquakes. *J. Geodyn.* **2019**, *124*, 1–13. [CrossRef]
12. Shi, K.; Ding, H.; Guo, J.; Yu, T. Refined seismic-ionospheric effects: Case study of Mw 8.2 Chiapas earthquake on September 7, 2017. *GPS Solut.* **2021**, *25*, 87. [CrossRef]
13. Li, Z.; Wang, N.; Li, M.; Zhou, K.; Yuan, Y.; Yuan, H. Evaluation and analysis of the global ionospheric TEC map in the frame of international GNSS services. *Chin. J. Geophys.* **2017**, *60*, 3718–3729. [CrossRef]
14. Solheim, F.; Vivekanandan, J.; Ware, R.; Rocken, C. Propagation delays induced in GPS signals by dry air, water vapor, hydrometeors, and other particulates. *J. Geophys. Res. Atmos.* **1999**, *104*, 9663–9670. [CrossRef]
15. Stoycheva, A.; Guerova, G. Study of fog in Bulgaria by using the GNSS tropospheric products and large-scale dynamic analysis. *J. Atmos. Sol.-Terr. Phys.* **2015**, *133*, 87–97. [CrossRef]
16. Pun, V.; Tian, L.; Ho, K. Particulate matter from re-suspended mineral dust and emergency cause-specific respiratory hospitalizations in Hong Kong. *Atmos. Environ.* **2017**, *165*, 191–197. [CrossRef]
17. Tang, X.; Hancock, C.M.; Xiang, Z.; Kong, Y.; de Ligt, H.; Shi, H.; Quaye-Ballard, J.A. Precipitable water vapour retrieval from GPS precise point positioning and NCEP CFSv2 dataset during typhoon events. *Sensors* **2018**, *18*, 3831. [CrossRef]
18. Guo, J.; Hou, R.; Zhou, M.; Jin, X.; Li, C.; Liu, X.; Gao, H. Monitoring 2019 forest fires in southeastern australia with GNSS technique. *Remote Sens.* **2021**, *13*, 386. [CrossRef]
19. Guo, J.; Hou, R.; Zhou, M.; Jin, X.; Li, G. Detection of particulate matter changes caused by 2020 California wildfires based on GNSS and radiosonde station. *Remote Sens.* **2021**, *13*, 4557. [CrossRef]

20. Wallace, L.; Beavan, J.; Bannister, S.; Williams, C. Simultaneous long-term and short-term slow slip events at the Hikurangi subduction margin, New Zealand: Implications for processes that control slow slip event occurrence, duration, and migration. *J. Geophys. Res. Solid Earth* **2021**, *117*, 402–419. [CrossRef]
21. Socquet, A.; Valdes, J.P.; Jara, J.; Cotton, F.; Walpersdorf, A.; Cotte, N.; Specht, S.; Ortega-Culaciati, F.; Carrizo, D.; Norabuena, E. An 8 month slow slip event triggers progressive nucleation of the 2014 Chile megathrust. *Geophys. Res. Lett.* **2017**, *44*, 4046–4053. [CrossRef]
22. Chen, G.; Wu, Y.; Jiang, Z.; Liu, X.; Zhao, J. Characteristics of seismogenic model of MW9.0 earthquake in Tohoku, Japan reflected by GPS data. *Chin. J. Geophys.* **2013**, *56*, 848–856. (In Chinese) [CrossRef]
23. Yue, H.; Lay, T. Inversion of high-rate (1 sps) GPS data for rupture process of the 11 March 2011 Tohoku earthquake (Mw 9.1). *Geophys. Res. Lett.* **2011**, *38*, L00G09. [CrossRef]
24. Blewitt, G.; Hammond, W.; Kreemer, C. Harnessing the GPS data explosion for interdisciplinary science. *Eos* **2018**, *99*, 485. [CrossRef]
25. Larson, K.; Levine, J. Carrier-phase time transfer. *IEEE Trans. Ultrason. Ferroelectr. Freq.* **1999**, *46*, 1001–1012. [CrossRef] [PubMed]
26. Saastamoinen, J. Atmospheric correction for the troposphere and stratosphere in radio ranging satellites. *Use Artif. Satell. Geod.* **1972**, *15*, 247–251. [CrossRef]
27. Hwang, C.; Peng, M.; Ning, J.; Luo, J.; Sui, C. Lake level variations in China from TOPEX/Poseidon altimetry: Data quality assessment and links to precipitation and ENSO. *Geophys. J. Int.* **2005**, *161*, 1–11. [CrossRef]
28. Huang, N.E.; Shen, Z.; Long, S.R.; Wu, M.C.; Shih, H.H.; Zheng, Q.; Yen, N.-C.; Tung, C.C.; Liu, H.H. The empirical mode decomposition and the Hilbert spectrum for nonlinear and non-stationary time series analysis. *Proc. R. Soc. Lond. Ser. A Math. Phys. Eng. Sci.* **1998**, *454*, 903–995. [CrossRef]
29. Wang, J.; Li, Z. Extreme-point symmetric mode decomposition method for data analysis. *Adv. Adapt. Data Anal.* **2003**, *5*, 1137. [CrossRef]
30. Calais, E.; Minster, J.; Hofton, M.; Hedlin, M. Ionospheric signature of surface mine blasts from Global Positioning System measurements. *Geophys. J. Int.* **1998**, *132*, 191–202. [CrossRef]